# Impact of Grid Carbon Intensity on the Multi-Objective Optimization of a PV–Battery–Hydrogen Hybrid Energy System

Aqib Khan[a], Mathieu Bressel[b], Arnaud Davigny[c], Dhaker Abbes[c] and Belkacem Ould Bouamama[b]

***Abstract*— This paper proposes a photovoltaic, battery, and hydrogen based hybrid energy system (HES) coordinated by a fuzzy logic based energy management system (FL-EMS) and optimized using a multi-objective NSGA-II algorithm. The objectives are to minimize annualized life cycle cost (ALCC), carbon emissions, and grid energy import index (EII). The impact of grid carbon intensity is assessed by comparing a low carbon French grid and a high carbon global grid.**

**Results show that grid carbon intensity significantly affects optimal design and operation. Under the low carbon grid, storage provides limited emission benefits, while under the high carbon grid, the system achieves up to 71% reduction in $CO_2$ emissions compared to the grid-only case. The FL-EMS adapts energy dispatch to balance cost, emissions, and autonomy.**

**The results highlight the trade-off between embodied and operational emissions and the strong dependence of optimal HES design on grid characteristics.**

***Index Terms*— Hybrid Energy System, Multi Objective Optimization, Grid Carbon Intensity, Fuzzy Logic Energy Management, Hydrogen Energy Storage, Lifecycle Emissions**

## I. Introduction

Renewable energy integration is essential for reducing greenhouse gas emissions, yet the variability of photovoltaic (PV) generation and the need to balance economic and environmental objectives pose significant design challenges [1], [2]. Hybrid Energy Systems (HES) combining PV, batteries, hydrogen storage, and grid interaction provide a promising solution, though their optimal design strongly depends on grid characteristics and environmental constraints [3], [4].

Most existing studies address system sizing, control strategies, or multi-objective optimization separately, rather than in an integrated framework. In addition, many works assume constant grid emission factors and neglect regional variability, which can significantly affect optimal configurations [5]–[7]. Lifecycle emissions of PV, batteries, and hydrogen components are also often overlooked despite their contribution to total emissions [8], [9].

This paper investigates a PV–battery–hydrogen HES coordinated by a fuzzy logic based energy management system (FL-EMS). A multi-objective NSGA-II algorithm is used to minimize the annualized life cycle cost (ALCC), carbon emissions ($CO_2$), and grid energy import index (EII). Unlike conventional approaches, grid carbon intensity is treated as a scenario-dependent parameter to evaluate its impact on system design and operation.

The main contributions are: (i) a joint optimization framework integrating system sizing and EMS parameter tuning, (ii) explicit inclusion of lifecycle emissions, considering both embodied and operational components, and (iii) a comparative analysis of low and high carbon grid scenarios to evaluate their impact on optimal configurations.

The remainder of the paper is organized as follows: Section 2 presents the system model and FL-EMS, Section 3 formulates the optimization problem, Section 4 presents the results, Section 5 provides discussion, and Section 6 concludes the paper.

## II. Hybrid Energy System Modeling and Fuzzy Logic Based Energy Management

The proposed HES comprises PV, battery, hydrogen system, and the utility grid, supplying a commercial building via a FL-EMS. System sizing and fuzzy controller parameters are jointly optimized to minimize ALCC, $CO_2$, and EII. Fig. 1 shows the overall architecture.

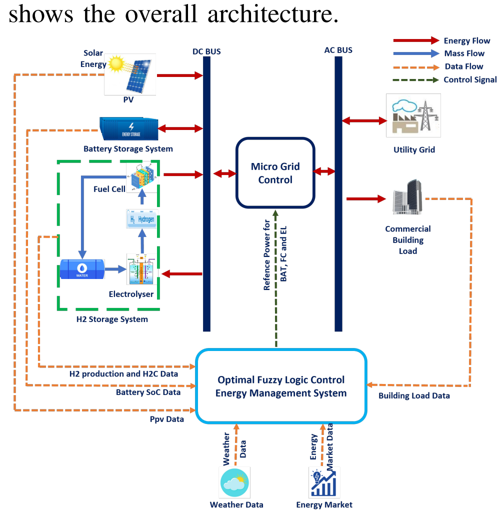


Fig. 1: Proposed PV–battery–hydrogen HES architecture.

### A. PV System

PV output power is modeled as [10]:

$$P_{PV}(t) = \eta_{PV}(t)\, A_{PV}\, I_r(t) \tag{1}$$

where $A_{PV}$ is the PV area (m$^2$), $I_r(t)$ the solar irradiance (W/m$^2$), and $\eta_{PV}(t)$ the effective efficiency, given by:

$$\eta_{PV}(t) = \eta_r\, \eta_{PC}\, \left[1 - \beta_t \left(T_c(t) - T_{STC}\right)\right] \tag{2}$$

[a]Aqib Khan (Corresponding Author) is with JUNIA - Grande Ecole d'ingénieurs, Université de Lille, CRIStAL - Centre de Recherche en Informatique Signal et Automatique de Lille, UMR 9189 CNRS, 59000, Lille, France aqib.khan.etu@univ-lille.fr aqib.khan@junia.com

[b]Mathieu Bressel and Belkacem Ould Bouamama are with Université de Lille, CRIStAL - Centre de Recherche en Informatique Signal et Automatique de Lille, UMR 9189 CNRS, 59650, Villeneuve D'Ascq, France mathieu.bressel@univ-lille.fr belkacem.ouldbouamama@polytech-lille.fr

[c] Arnaud Davigny and Dhaker Abbes are with JUNIA - Grande Ecole d'ingénieurs, Univ. Lille, Arts et Métiers Institute of Technology, Centrale Lille, Junia, ULR 2697 – L2EP F-59000 Lille, France arnaud.davigny@junia.com dhaker.abbes@junia.com

where $\eta_r$, $\eta_{PC}$, $\beta_t$, $T_c(t)$, and $T_{STC} = 25°\text{C}$ are the reference efficiency, performance ratio, temperature coefficient, cell temperature, and standard test temperature, respectively.

### *B. Battery Storage System*

A lithium-ion battery is modeled using an equivalent circuit [11]:

$$V_{bat}(t) = E_b(t) - R_o I_{bat}(t) \tag{3}$$

$$E_b(t) = E_0 - \frac{KQ}{Q - I_{bat}(t)t}\left(I_{bat}(t) + I^*\right) + Ae^{-BI_{bat}(t)} \tag{4}$$

$$SoC_{bat}(t + \Delta t) = SoC_{bat}(t) + \eta_{ch/dis}\frac{I_{bat}(t)\Delta t}{Q} \tag{5}$$

where $V_{bat}$, $E_b$, $R_o$, $I_{bat}$, $E_0$, $K$, $Q$, $A$, $B$, $I^*$, and $\eta_{ch/dis}$ are the terminal voltage, open-circuit voltage, internal resistance, current, fully charged voltage, polarization constant, nominal capacity, exponential parameters, filtered polarization current, and charge-discharge efficiency, respectively.

### *C. Hydrogen System*

The hydrogen system consists of a Proton Exchange Membrane (PEM) electrolyzer, storage tank, and PEM fuel cell. The fuel cell and electrolyzer voltages share the same overpotential structure [12]:

$$V_{FC}(t) = E_{th}(t) - \eta_{act}(t) - \eta_{diff}(t) - \eta_{ohm}(t) \tag{6}$$

$$V_{EL}(t) = E_{th}(t) + \eta_{act}(t) + \eta_{diff}(t) + \eta_{ohm}(t) \tag{7}$$

where $E_{th}$, $\eta_{act}$, $\eta_{diff}$, and $\eta_{ohm} = I_{FC}R_{tot}$ are the thermodynamic, activation, diffusion, and ohmic terms, respectively, with:

$$E_{th} = E_0 + \frac{RT_{FC}}{nF}\ln\left(\frac{P_{H_2}\sqrt{P_{O_2}}}{P_{H_2O}}\right) \tag{8}$$

$$\eta_{act} = AT_{FC}\ln\left(\frac{I_{FC} + I_{crossover}}{I_0}\right) \tag{9}$$

$$\eta_{diff} = BT_{FC}\ln\left(1 - \frac{I_{FC} + I_{crossover}}{I_{lim}}\right) \tag{10}$$

Tank dynamics and hydrogen state of charge are given by:

$$\frac{dm_{stored}}{dt} = \dot{m}_{in} - \dot{m}_{out}, \qquad H2C(t) = \frac{P_{HST}(t)}{P_{NWP}} \tag{11}$$

where $P_{HST}(t)$ and $P_{NWP}$ are the instantaneous and nominal working pressures [12].

### *D. Commercial Building Load*

Measured hourly load data from a French commercial site for year 2022 captures realistic daily and seasonal variations. Fig. 2 shows a representative one-week profile.

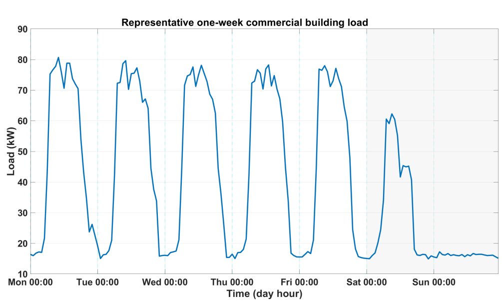


Fig. 2: Representative one-week building load profile (kW).

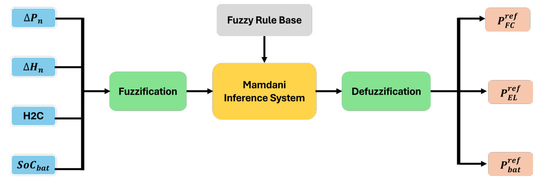


Fig. 3: Fuzzy logic control structure of the energy management system.

### *E. Fuzzy Logic-Based Energy Management System*

A Mamdani-type fuzzy logic controller (FLC) is designed to manage energy flows in the hybrid system, as illustrated in Fig. 3. The input variables are selected to capture both power balance and storage dynamics.

The controller uses four inputs: normalized power imbalance $\Delta P_n$, hydrogen imbalance $\Delta H_n$, battery state of charge $SoC_{bat}$, and hydrogen capacity $H2C$, to generate reference signals for the battery ($P_{bat}^{ref}$), electrolyzer ($P_{EL}^{ref}$), and fuel cell ($P_{FC}^{ref}$). The power and hydrogen imbalances are normalized using a hyperbolic tangent function to ensure bounded and smooth control behavior: reducing abrupt variations in control actions.

$$\Delta P_n = \tanh(\Delta P), \quad \Delta H_n = \tanh(\Delta H) \tag{12}$$

Triangular and trapezoidal membership functions are used for computational efficiency and smooth transitions. The inputs $\Delta P_n$ and $\Delta H_n$ have three linguistic levels (negative, zero, positive), while $SoC_{bat}$ and $H2C$ use low, medium, and high states. The fuzzy inference system includes fuzzification, rule evaluation with the max operator, and centroid defuzzification. The rule base contains 31 rules, with a representative subset shown in Table I.

TABLE I: Representative fuzzy rule base

| $\Delta P_n$ | $\Delta H_n$ | SoC | $H_2C$ | FC | EL | BAT |
|---|---|---|---|---|---|---|
| P | – | H | H | OFF | OFF | Idle |
| P | – | M | L | OFF | ON | Charge |
| Z | – | – | – | OFF | OFF | Idle |
| N | P | H | H | ON | OFF | Discharge |
| N | – | M | L | OFF | OFF | Discharge |
| N | – | L | L | OFF | OFF | Idle |

P: Positive, N: Negative, L: Low, M: Medium, H: High

The EMS follows a hierarchical strategy where PV generation first supplies the load, then charges the battery and powers the electrolyzer, with excess energy exported to the grid. During deficits, the battery discharges first, followed

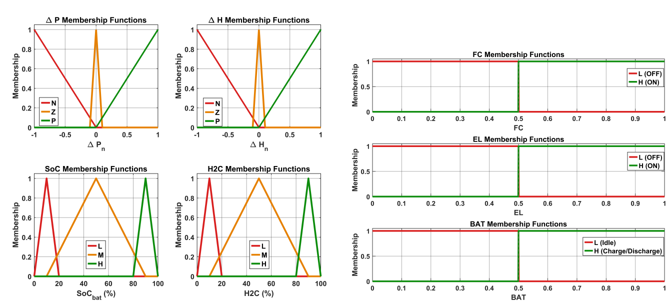


(a) Input (b) Output

Fig. 4: Membership functions of the fuzzy logic controller.

by fuel cell activation when hydrogen is available, and the grid covers the remaining demand. The fuzzy rules enforce these priorities, ensuring a balanced trade-off between cost, emissions, and energy autonomy.

## III. Joint Multi-Objective Optimization of Component Sizing and Fuzzy EMS

The optimization problem considers three objectives: ALCC, $CO_2$, and EII. The NSGA-II algorithm is used to explore the trade-offs among them. The decision vector includes both system sizing and fuzzy EMS parameters, capturing their strong interdependence. The EMS influences energy dispatch, which in turn affects optimal component sizing. This coupling is explicitly considered to ensure coordinated design and control.

### A. Decision Variables

The optimization vector combines system sizing and fuzzy logic parameters:

$$\mathbf{x} = [\mathbf{x}_1, \mathbf{x}_2] \in \mathbb{R}^{13} \tag{13}$$

where

$$\mathbf{x}_1 = [A_{\mathrm{PV}}, Q_{\mathrm{bat}}, Q_{\mathrm{H2\_tank}}, P_{\mathrm{FC}}, P_{\mathrm{EL}}]$$

$$\mathbf{x}_2 = [\alpha_1, \alpha_2, \alpha_3, \alpha_4, \beta_1, \beta_2, \beta_3, \beta_4]$$

The two subsets are strongly coupled, since the fuzzy membership breakpoints directly influence storage activation, affecting energy flows and overall system performance. Only the membership function breakpoints associated with $SoC_{bat}$ and H2C are optimized, while the fuzzy rule base remains unchanged and the membership ordering is preserved through bounded constraints. The corresponding parameterization is summarized in Table II.

TABLE II: Triangular membership functions for $SoC_{bat}$ and H2C (%)

| Level | H2C | | $SoC_{bat}$ | |
|---|---|---|---|---|
| | Initial | Optimized | Initial | Optimized |
| L | [0,10,20] | [0,10,$\alpha_1$] | [0,10,20] | [0,10,$\beta_1$] |
| M | [10,50,90] | [10,$\alpha_2$,$\alpha_4$] | [10,50,90] | [10,$\beta_2$,$\beta_4$] |
| H | [80,90,100] | [$\alpha_3$,$\alpha_4$,100] | [80,90,100] | [$\beta_3$,$\beta_4$,100] |

Optimized parameters $\alpha_i$ and $\beta_i$ are constrained within $[10, 90]$ to preserve meaningful fuzzy partitions and avoid boundary degeneration.

### B. Objective Functions

Three conflicting objectives are considered.

**1) Annualized Life-Cycle Cost (ALCC):**

$$\mathrm{ALCC} = \mathrm{CRF} \cdot \mathrm{NPC}_{\mathrm{sys}}, \quad \mathrm{CRF} = \frac{r(1+r)^N}{(1+r)^N - 1} \tag{14}$$

where $\mathrm{NPC}_{\mathrm{sys}}$ includes capital, replacement, O&M, and grid costs over the lifetime $N$.

**2) Total Carbon Emissions:**

$$CO_2^{\mathrm{total}} = CO_2^{\mathrm{grid}} + CO_2^{\mathrm{PV}} + CO_2^{\mathrm{bat}} + CO_2^{\mathrm{H2}} \tag{15}$$

Grid emissions are computed from hourly imports:

$$CO_2^{\mathrm{grid}} = \sum_{t=1}^{T} P_{\mathrm{grid}}(t)\,\Delta t \cdot CO_{2,\mathrm{grid}} \tag{16}$$

while embodied emissions are annualized over component lifetimes:

$$CO_2^{\mathrm{PV}} = \frac{A_{\mathrm{PV}} \cdot CO_{2,\mathrm{PV}}}{L_{\mathrm{PV}}}, \quad CO_2^{\mathrm{bat}} = \frac{Q_{\mathrm{bat}} \cdot CO_{2,\mathrm{bat}}}{L_{\mathrm{bat}}} \tag{17}$$

$$CO_2^{\mathrm{H2}} = \frac{Q_{\mathrm{H2,tank}} \cdot CO_{2,\mathrm{tank}}}{L_{\mathrm{H2,tank}}} + \frac{P_{\mathrm{FC}} \cdot CO_{2,\mathrm{FC}}}{L_{\mathrm{FC}}} + \frac{P_{\mathrm{EL}} \cdot CO_{2,\mathrm{EL}}}{L_{\mathrm{EL}}} \tag{18}$$

**3) Energy Import Index (EII):** EII quantifies grid energy dependence as the ratio of imported grid energy to total load demand:

$$\mathrm{EII} = \frac{\sum_{t=1}^{T} P_{\mathrm{grid}}^{\mathrm{import}}(t)\Delta t}{\sum_{t=1}^{T} P_{\mathrm{load}}(t)\Delta t} \in [0, 1], \tag{19}$$

where $P_{\mathrm{grid}}^{\mathrm{import}}(t) = \max(P_{\mathrm{grid}}(t), 0)$. A value of 0 indicates full autonomy, while 1 indicates full grid dependence. Therefore, a reduction in EII corresponds to an improvement in system autonomy.

The optimization problem is formulated as:

$$\min_{\mathbf{x} \in \mathcal{X}} \mathbf{F}(\mathbf{x}) = [\mathrm{ALCC},\ CO_2^{\mathrm{total}},\ \mathrm{EII}] \tag{20}$$

subject to the bound and operational constraints:

$$\mathbf{x}_{\mathrm{lb}} \le \mathbf{x} \le \mathbf{x}_{\mathrm{ub}}, \tag{21}$$

$$10\% \le SoC_{bat} \le 90\%, \quad 10\% \le H2C \le 90\% \tag{22}$$

$$P_{PV}(t) + P_{grid}(t) + P_{FC}(t) = P_{Load}(t) + P_{EL}(t) + P_{bat}(t) \tag{23}$$

### C. Pareto Front Analysis

The multi-objective problem is solved using NSGA-II, yielding a Pareto-optimal set $\mathcal{P}$. Four representative solutions are selected:

- **Solution I – Minimum Cost:**
$$\mathbf{x}^{\mathrm{I}} = \arg\min_{\mathbf{x} \in \mathcal{P}} \mathrm{ALCC}(\mathbf{x})$$
- **Solution II – Minimum Carbon:**
$$\mathbf{x}^{\mathrm{II}} = \arg\min_{\mathbf{x} \in \mathcal{P}} CO_2^{\mathrm{total}}(\mathbf{x})$$
- **Solution III – Minimum Energy Import:**
$$\mathbf{x}^{\mathrm{III}} = \arg\min_{\mathbf{x} \in \mathcal{P}} \mathrm{EII}(\mathbf{x})$$
- **Solution IV – Compromise:** This solution provides a balanced trade-off among the three objectives. It is obtained by minimizing the average of normalized objectives over the Pareto set:
$$\mathbf{x}^{\mathrm{IV}} = \arg\min_{\mathbf{x} \in \mathcal{P}} \frac{1}{3} \sum_{i=1}^{3} \frac{f_i(\mathbf{x})}{\max_{\mathbf{x} \in \mathcal{P}} f_i(\mathbf{x})}$$
This ensures a fair balance between ALCC, $CO_2$, and EII.

## IV. Simulation Setup and Results

This section presents the simulation setup, optimization results, and analysis of the proposed PV–battery–hydrogen HES under two grid carbon intensity scenarios.

### A. Simulation Setup

The optimization follows a structured workflow. System data, load profiles, and tariff inputs are first defined. A 13-dimensional decision vector is then constructed, comprising system sizing variables and FL-EMS parameters. Annual simulations are performed using a MATLAB/Simulink model at hourly resolution. Three objectives are evaluated: ALCC, $CO_2^{\mathrm{total}}$ and EII. The NSGA-II algorithm generates the Pareto front, from which four representative solutions are selected for analysis.

A representative commercial building in France is considered, using measured load and meteorological data. Dynamic

Blue, Yellow, and Green tariffs from the French electricity market are applied according to grid subscription levels [13]. The same tariff structure is used across both scenarios so that differences in results can be attributed solely to grid carbon intensity.

Techno-economic parameters and embodied carbon coefficients are summarized in Tables III and IV. A discount rate of $r = 5\%$ and a project lifetime of $N = 25$ years are assumed [14]–[22].

TABLE III: Techno-economic parameters ($r = 5\%$, $N = 25$ yr) [14]–[16]

| Component | Unit | Cost | O&M/yr | Lifetime | Bounds |
|---|---|---|---|---|---|
| PV array | $m^2$ | 200 EUR/$m^2$ | 1 EUR/$m^2$ | 25 yr | 1 – 2000 |
| Li-ion battery | Ah (at $V_{\mathrm{nom}} = 48$ V) | 5 EUR/Ah | 0.15 EUR/Ah | 10 yr | 420 – 84,000 |
| $H_2$ tank | $m^3$ | 625 EUR/$m^3$ | 10 EUR/$m^3$ | 30 yr | 4 – 20.4 |
| PEM fuel cell | kW | 400 EUR/kW | 8 EUR/kW | 15 yr | 6 – 120 |
| PEM electrolyzer | kW | 650 EUR/kW | 5 EUR/kW | 15 yr | 8 – 160 |

TABLE IV: Embodied carbon coefficients and operational grid emission factors [17]–[22]

| Component / Source | Value | Unit |
|---|---|---|
| French grid (operational) | 0.039 | kg $CO_2$/kWh |
| Global grid (operational) | 0.454 | kg $CO_2$/kWh |
| PV array (embodied) | 129.93 | kg $CO_2$/$m^2$ |
| Li-ion battery (embodied) | 6.78 | kg $CO_2$/Ah |
| $H_2$ tank (embodied) | 80 | kg $CO_2$/$m^3$ |
| PEM fuel cell (embodied) | 62.5 | kg $CO_2$/kW |
| PEM electrolyzer (embodied) | 80 | kg $CO_2$/kW |

Simulations are performed on a 13th Gen Intel Core i7 13700K (3.40 GHz) with 32 GB RAM using MATLAB `parpool` with 12 workers. The NSGA II algorithm is implemented using `gamultiobj` with 130 individuals and 100 generations, enabling parallel computation and direct coupling with the Simulink based model. Crossover and mutation operators ensure diversity and convergence, while constraint handling follows the feasibility rule.

Two grid carbon intensity scenarios are compared: a low-carbon French grid (39 g $CO_2$/kWh) and a high-carbon global average grid (454 g $CO_2$/kWh), the latter being approximately 11.6× higher. The corresponding grid-only baselines are 14,988 and 174,472 kg $CO_2$/yr, respectively, serving as benchmarks. The same French electricity pricing is applied in both cases to isolate the effect of carbon intensity.

### B. Pareto Front Analysis

The multi-objective optimization results are presented as Pareto fronts in the ALCC–$CO_2^{\mathrm{total}}$–EII space. Fig. 5 shows two-dimensional projections for both grid scenarios.

In the ALCC–$CO_2^{\mathrm{total}}$ plane, the global grid Pareto front is shifted substantially upward relative to the French grid front, indicating that grid carbon intensity has a dominant influence on achievable emissions at any given cost. In the ALCC–EII plane, the two fronts are nearly coincident, suggesting that EII is mainly constrained by system sizing limits rather than emission factors

Table V summarizes the objective ranges across both scenarios. The global grid yields higher emissions and a wider ALCC range, while the EII range remains relatively narrow, reflecting the physical limitations imposed by system sizing constraints.

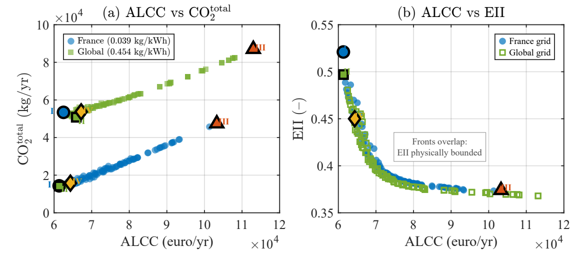


Fig. 5: MOGA Pareto fronts under France and global grids. (a) ALCC vs $CO_2^{\mathrm{total}}$: separated fronts. (b) ALCC vs EII: overlapping fronts.

TABLE V: MOGA Pareto front objective ranges under France and global grids, based on Solutions I–IV.

| Indicator | France grid | Global grid |
|---|---|---|
| Min ALCC (EUR/yr) | 61 342 (Sol. I) | 62 500 (Sol. I) |
| Max ALCC (EUR/yr) | 103 280 (Sol. III) | 113 000 (Sol. III) |
| ALCC range (EUR/yr) | 41 938 | 50 500 |
| Min $CO_2$ (kg/yr) | 14 207 (Sol. II) | 50 800 (Sol. II) |
| Max $CO_2$ (kg/yr) | 47 431 (Sol. III) | 87 000 (Sol. III) |
| $CO_2$ range (kg/yr) | 33 224 | 36 200 |
| Min EII | 0.374 (Sol. III) | 0.371 (Sol. III) |
| Max EII | 0.521 (Sol. I) | 0.481 (Sol. I) |
| EII range | 0.147 | 0.110 |

### C. Representative Pareto Solutions

Table VI presents the four representative Pareto solutions under each grid scenario. Fig. 6 provides a direct comparison of ALCC, $CO_2^{\mathrm{total}}$, and EII relative to the respective grid-only baselines; Fig. 7 compares optimal component sizing across all solutions.

TABLE VI: Representative Pareto solutions under France (0.039 kg/kWh) and global (0.454 kg/kWh) grids.

| | France grid (0.039 kg/kWh) | | | | Global grid (0.454 kg/kWh) | | | |
|---|---|---|---|---|---|---|---|---|
| Indicator | Sol. I | Sol. II | Sol. III | Sol. IV | Sol. I | Sol. II | Sol. III | Sol. IV |
| *Optimal sizing* | | | | | | | | |
| $A_{\mathrm{PV}}$ ($m^2$) | 1 760 | 1 947 | 1 980 | 1 964 | 1 933 | 1 978 | 1 975 | 1 976 |
| $Q_{\mathrm{bat}}$ (Ah) | 1 030 | 1 075 | 49 636 | 2 560 | 866 | 1 482 | 62 205 | 4 790 |
| $Q_{\mathrm{H2\_tank}}$ ($m^3$) | 4.87 | 5.62 | 16.57 | 10.40 | 7.41 | 16.25 | 20.03 | 14.17 |
| $P_{\mathrm{FC}}$ (kW) | 12.90 | 13.25 | 101.93 | 25.18 | 11.11 | 76.04 | 94.51 | 60.88 |
| $P_{\mathrm{EL}}$ (kW) | 13.57 | 13.74 | 21.13 | 25.64 | 24.95 | 23.83 | 23.27 | 23.97 |
| *FL-EMS parameters (%)* | | | | | | | | |
| $\alpha_1$ | 20.79 | 21.89 | 16.52 | 17.93 | 22.09 | 19.11 | 17.85 | 17.81 |
| $\alpha_2$ | 24.43 | 35.88 | 61.13 | 32.44 | 37.05 | 45.14 | 49.88 | 38.22 |
| $\alpha_3$ | 27.02 | 37.88 | 66.28 | 46.23 | 53.58 | 62.51 | 70.43 | 68.84 |
| $\alpha_4$ | 29.02 | 40.84 | 68.28 | 48.23 | 60.25 | 68.15 | 75.40 | 72.81 |
| $\beta_1$ | 17.18 | 29.51 | 41.67 | 27.69 | 33.59 | 32.74 | 33.26 | 31.01 |
| $\beta_2$ | 25.86 | 31.86 | 48.78 | 32.88 | 35.59 | 35.71 | 36.57 | 35.82 |
| $\beta_3$ | 28.93 | 45.88 | 52.97 | 52.17 | 43.86 | 72.87 | 74.60 | 73.40 |
| $\beta_4$ | 44.42 | 52.21 | 72.57 | 69.34 | 55.72 | 74.87 | 76.60 | 75.40 |
| *Performance indicators* | | | | | | | | |
| NPC (k EUR) | 864.55 | 864.96 | 1 455.70 | 906.79 | 881.00 | 929.00 | 1 600.00 | 947.00 |
| ALCC (EUR/yr) | 61 342 | 61 371 | 103 280 | 64 339 | 62 500 | 65 900 | 113 000 | 67 200 |
| LCOE (EUR/kWh) | 0.1596 | 0.1597 | 0.2688 | 0.1674 | 0.1626 | 0.1715 | 0.2950 | 0.1749 |
| $CO_2^{\mathrm{total}}$ (kg/yr) | 14 340 | 14 207 | 47 431 | 15 764 | 53 400 | 50 800 | 87 000 | 53 700 |
| EII | 0.521 | 0.497 | 0.374 | 0.450 | 0.481 | 0.456 | 0.371 | 0.414 |

The results indicate that higher grid carbon intensity drives greater renewable penetration and increased storage utilization. Under the global grid, PV capacity reaches its upper bound and hydrogen storage increases in emission-focused solutions, as reducing reliance on carbon-intensive grid electricity becomes the dominant optimization driver.

### D. FL-EMS Co-Optimization Contribution

The contribution of jointly optimizing FL EMS parameters alongside system sizing is evaluated by comparing Config-S (sizing only) and Config-J (joint optimization).

Table VII summarizes sizing, FL-EMS parameters, and performance for both configurations.

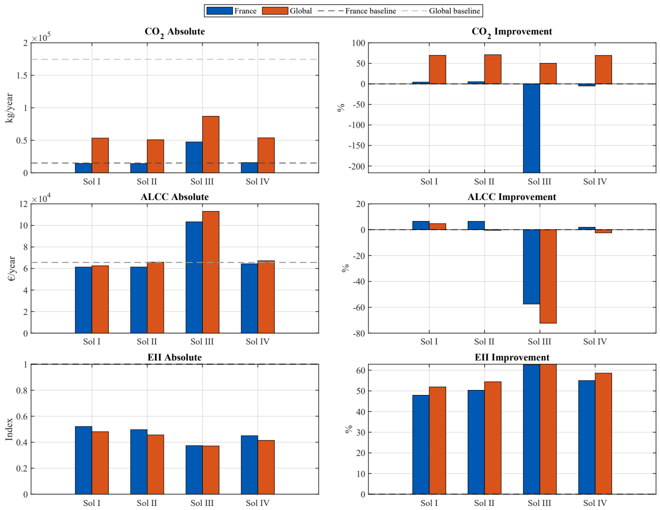


Fig. 6: $CO_2^{\mathrm{total}}$, ALCC, and EII for Solutions I–IV under France and global grids, relative to grid-only baselines.

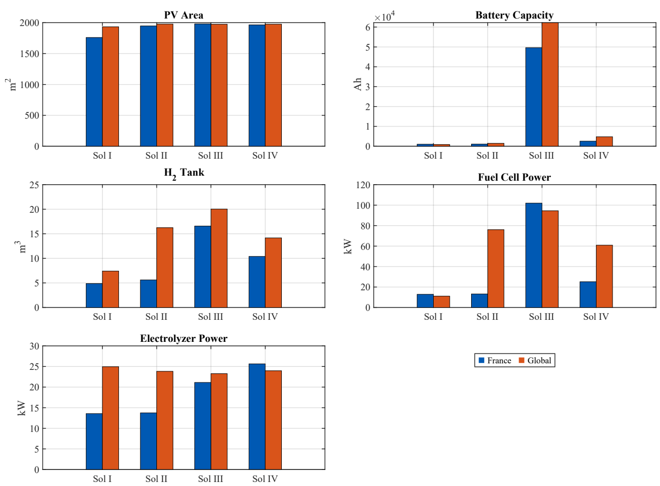


Fig. 7: Optimal component sizing for Solutions I–IV under France and global grids.

TABLE VII: Config-S (sizing only, 5D) vs. Config-J (joint sizing and control, 13D) for the France grid scenario.

| | | Config-S (Sizing only, 5D) | | | | Config-J (Joint, 13D) | | | |
|---|---|---|---|---|---|---|---|---|---|
| Indicator | Unit | Sol. I | Sol. II | Sol. III | Sol. IV | Sol. I | Sol. II | Sol. III | Sol. IV |
| *Optimal sizing* | | | | | | | | | |
| $A_{\mathrm{PV}}$ | m$^2$ | 1,758 | 1,873 | 1,978 | 1,970 | 1,760 | 1,947 | 1,980 | 1,964 |
| $Q_{\mathrm{bat}}$ | Ah | 1,887 | 1,493 | 50,485 | 5,653 | 1,030 | 1,075 | 49,636 | 2,560 |
| $Q_{\mathrm{H2\_tank}}$ | m$^3$ | 11.81 | 11.89 | 15.24 | 14.13 | 4.87 | 5.62 | 16.57 | 10.40 |
| $P_{\mathrm{FC}}$ | kW | 8.75 | 12.87 | 99.26 | 30.18 | 12.90 | 13.25 | 101.93 | 25.18 |
| $P_{\mathrm{EL}}$ | kW | 15.47 | 17.57 | 17.53 | 17.56 | 13.57 | 13.74 | 21.13 | 25.64 |
| *FL-EMS parameters (%) — Config-J only* | | | | | | | | | |
| $\alpha_1$ | % | fixed (20) | | | | 20.79 | 21.89 | 16.52 | 17.93 |
| $\alpha_2$ | % | fixed (50) | | | | 24.43 | 35.88 | 61.13 | 32.44 |
| $\alpha_3$ | % | fixed (80) | | | | 27.02 | 37.88 | 66.28 | 46.23 |
| $\alpha_4$ | % | fixed (90) | | | | 29.02 | 40.84 | 68.28 | 48.23 |
| $\beta_1$ | % | fixed (20) | | | | 17.18 | 29.51 | 41.67 | 27.69 |
| $\beta_2$ | % | fixed (50) | | | | 25.86 | 31.86 | 48.78 | 32.88 |
| $\beta_3$ | % | fixed (80) | | | | 28.93 | 45.88 | 52.97 | 52.17 |
| $\beta_4$ | % | fixed (90) | | | | 44.42 | 52.21 | 72.57 | 69.34 |
| *Performance* | | | | | | | | | |
| NPC | k€ | 876.04 | 878.22 | 1,458.71 | 927.50 | 864.55 | 864.96 | 1,455.70 | 906.79 |
| ALCC | €/yr | 62,157 | 62,312 | 103,499 | 65,808 | 61,342 | 61,371 | 103,280 | 64,339 |
| LCOE | €/kWh | 0.1617 | 0.1621 | 0.2693 | 0.1712 | 0.1596 | 0.1597 | 0.2688 | 0.1674 |
| $CO_2$ | kg/yr | 15,020 | 14,753 | 47,958 | 17,671 | 14,340 | 14,207 | 47,431 | 15,764 |
| EII | – | 0.495 | 0.483 | 0.372 | 0.416 | 0.521 | 0.497 | 0.374 | 0.450 |
| *Δ: Config-J vs. Config-S* | | | | | | | | | |
| ΔALCC | €/yr | – | | | | −815 | −941 | −219 | −1,469 |
| ΔALCC | % | – | | | | −1.31 | −1.51 | −0.21 | −2.23 |
| $\Delta CO_2$ | % | – | | | | −4.53 | −3.70 | −1.10 | −10.79 |

These results confirm that co optimization improves both economic and environmental performance, although the magnitude of improvement depends on the level of operational flexibility. In the France grid scenario, ALCC is reduced by up to 2.23% and $CO_2$ emissions by up to 10.79%.

In contrast, improvements are limited for highly constrained solutions where system sizing dominates performance, reducing the impact of control optimization.

## V. Results Discussion

Grid carbon intensity plays a critical role in shaping optimal system configurations and operational strategies, leading to distinct trade-offs between cost, emissions, and grid dependence.

### A. Impact of Grid Carbon Intensity on System Sizing

Grid carbon intensity has a significant impact on optimal component sizing. Under the low carbon French grid, cost optimal solutions select moderate PV sizes and relatively small battery capacities. Due to the low emission factor, additional storage provides limited environmental benefit and is not economically justified.

Under the global grid, PV capacity approaches its upper bound across all solutions, and hydrogen storage increases significantly. Fuel cell capacity also increases in emission-focused solutions, reflecting the need for dispatchable generation to reduce reliance on high-emission grid electricity.

### B. Embodied vs. Operational Carbon Trade-Off

A key observation is the trade-off between embodied carbon and operational emissions. Under the French grid, the grid-only baseline is already very low in emissions. Thus, adding large storage systems increases lifecycle emissions due to embodied carbon, which can outweigh operational benefits.

This leads to the counterintuitive result where Solution III produces higher emissions than the grid-only baseline. This highlights the importance of lifecycle-based design rather than focusing solely on energy independence.

Under the global grid, the situation reverses. Avoided grid electricity becomes the dominant source of emission reduction, and all solutions achieve significant $CO_2$ reductions, typically in the range of 69–71%.

### C. EII Behavior and Physical Bounds

The energy independence index shows limited variation across grid scenarios. This confirms that EII is mainly constrained by system sizing rather than grid emission factors.

Even in the most independent solution, a significant portion of energy is still supplied by the grid, indicating that complete self sufficiency is not achievable under the considered constraints.

### D. FL-EMS Adaptation to Grid Carbon Context

The fuzzy logic-based EMS adapts through optimized $\alpha$ and $\beta$ parameters defining $H_2C$ and SoC membership functions. Since the electrolyzer operates when $H_2C$ is Low or Medium, upward shifts in $\alpha$ reshape these regions to favor operation under higher PV surplus, ensuring renewable-driven hydrogen production. Similarly, increased $\beta$ values promote higher battery reserves, reducing grid dependence during low PV periods. These adjustments show that optimization refines both sizing and control strategy.

### *E. Deployment Relevance*

The results highlight different deployment opportunities depending on grid carbon intensity.

Under the French grid, the hybrid system achieves modest emission reductions with minimal cost variation across solutions.

Under the global grid, the system achieves substantial emission reductions while remaining economically competitive, with up to 69.4% $CO_2$ reduction and only a 1.9% increase in ALCC for the best trade-off solution.

These results confirm that the framework adapts effectively to different grid carbon intensities without structural modification. The emission factor is the primary scenario-dependent input, while the system model and EMS remain unchanged.

This enables direct deployment across regions with varying carbon intensities, while allowing optimization of both sizing and control strategies.

## VI. Conclusion and Future Work

This paper presented a PV–battery–hydrogen HES with a fuzzy logic based EMS, optimized using a multi-objective NSGA-II framework. The results demonstrate that grid carbon intensity significantly influences both optimal system sizing and operational strategies.

Quantitative results show that under a high carbon grid, the proposed system can achieve up to 71% reduction in $CO_2$ emissions compared to the grid-only baseline, while under a low carbon grid, the benefits of additional storage are limited due to the dominance of embodied emissions.

A key contribution of this work is the identification of the trade-off between embodied and operational emissions, highlighting that energy independence does not always lead to lower lifecycle emissions.

The proposed framework effectively captures the trade offs between cost, emissions, and grid dependence, while maintaining adaptability across different grid scenarios without structural changes.

Future work will extend the model by incorporating additional renewable energy sources, evaluating multiple building types and geographic regions, and including component degradation to improve long term accuracy and robustness.

## Acknowledgment

This work was funded by the French National Agency for Research through the COSMAC project (ANR-22-CE05-0013, Optimal Design of a Multi-Energy System Applied to Commercial Buildings).

## References

[1] S. Bakhsh, W. Zhang, K. Ali, and J. Oláh, "Strategy towards sustainable energy transition: The effect of environmental governance, economic complexity and geopolitics," *Energy Strategy Reviews*, vol. 52, p. 101330, 2024.

[2] A. Khan, M. Bressel, A. Davigny, D. Abbes, and B. Ould Bouamama, "Comprehensive review of hybrid energy systems: Challenges, applications, and optimization strategies," *Energies*, vol. 18, no. 10, 2025.

[3] J. Liu, X. Chen, H. Yang, and K. Shan, "Hybrid renewable energy applications in zero-energy buildings and communities integrating battery and hydrogen vehicle storage," *Applied Energy*, vol. 290, p. 116733, 2021.

[4] G. Yang, D. Yang, B. Liu, and H. Zhang, "The role of short- and long-duration energy storage in reducing the cost of firm photovoltaic generation," *Applied Energy*, vol. 374, p. 123914, 2024.

[5] R. Wang and R. Zhang, "Techno-economic analysis and optimization of hybrid energy systems based on hydrogen storage for sustainable energy utilization by a biological-inspired optimization algorithm," *Journal of Energy Storage*, vol. 66, p. 107469, 2023.

[6] M. J. Mayer, A. Szilágyi, and G. Gróf, "Environmental and economic multi-objective optimization of a household level hybrid renewable energy system by genetic algorithm," *Applied Energy*, vol. 269, p. 115058, 2020.

[7] A. Maheri, I. Unsal, and O. Mahian, "Multiobjective optimisation of hybrid wind-PV-battery-fuel cell-electrolyser-diesel systems: An integrated configuration-size formulation approach," *Energy*, vol. 241, p. 122825, Feb. 2022.

[8] A. Khan, M. Bressel, A. Davigny, D. Abbes, and B. O. Bouamama, "A comparative study of genetic algorithm and particle swarm optimization for hybrid renewable systems with battery and hydrogen system," in *The 26th European Conference on Power Electronics and Applications*, 2025.

[9] B. K. Das, R. Hassan, M. S. H. Tushar, F. Zaman, M. Hasan, and P. Das, "Techno-economic and environmental assessment of a hybrid renewable energy system using multi-objective genetic algorithm: A case study for remote island in bangladesh," *Energy Conversion and Management*, vol. 230, p. 113823, 2021.

[10] A. Khan, M. Bressel, D. Abbes, A. Davigny, and B. O. Bouamama, "Green energy integration: Modeling photovoltaic, hydrogen, and battery systems for cost and carbon emission reduction in micro-grids," in *2024 12th International Conference on Systems and Control (ICSC)*, Nov 2024, pp. 295–300.

[11] S. Lavety, R. K. Keshri, and M. A. Chaudhari, "A dynamic battery model and parameter extraction for discharge behavior of a valve regulated lead-acid battery," *Journal of Energy Storage*, vol. 33, p. 102031, 2021.

[12] A. Hervé and M. Bressel, "Optimal sizing of isolated photovoltaic-hydrogen microgrids using covariance matrix adaptation evolution strategy considering real-gas modeling of hydrogen," *Applied Energy*, vol. 401, p. 126677, 2025.

[13] EDF, "Edf fr, tarif bleu, jaune, vert : éligibilité, tarifs, alternatives. dec. 29, 2025." https://www.edf.fr/entreprises/tarifs-reglementes-de-vente.

[14] IRENA, "Renewable power generation costs in 2023," International Renewable Energy Agency, Abu Dhabi, Tech. Rep., 2024. [Online]. Available: https://www.irena.org

[15] US DOE Fuel Cell Technologies Office, "Clean hydrogen production cost: PEM electrolyzer," US Department of Energy, Tech. Rep. 24005, 2024. [Online]. Available: https://www.hydrogen.energy.gov

[16] IEA, "Global hydrogen review 2023," International Energy Agency, Paris, Tech. Rep., 2023. [Online]. Available: https://www.iea.org/reports/ global-hydrogen-review-2023

[17] RTE, "French annual electricity review 2023," Réseau de Transport d'Electricité, Paris, Tech. Rep., 2024. [Online]. Available: https://analysesetdonnees.rte-france.com/ en/annual-review-2023

[18] IEA, "Emissions factors 2024," 2024. [Online]. Available: https://www.iea.org/data-and-statistics/ data-product/emissions-factors-2024

[19] IEA PVPS Task 12, "Environmental life cycle assessment of electricity from PV systems," IEA Photovoltaic Power Systems Programme, Tech. Rep. T12-23, 2022. [Online]. Available: https://iea-pvps.org

[20] T. Le Varlet, O. Schmidt, A. Gambhir, S. Few, and I. Staffell, "Comparative life cycle assessment of lithium-ion battery chemistries for residential storage," *Journal of Energy Storage*, vol. 28, p. 101286, 2020.

[21] IEA(2023), "Comparison of the emissions intensity of different hydrogen production routes, 2021," https://www.iea.org/data-and-statistics/charts/comparison-of-the-emissions-intensity-of-different-hydrogen-production-routes-2021.

[22] A. Valente, D. Iribarren, and J. Dufour, "Life cycle assessment of hydrogen energy systems: a review of methodological choices," *International Journal of Hydrogen Energy*, vol. 46, pp. 31 543–31 571, 2021.